

1 **Selective laser melted AlSi10Mg alloy under melting mode**
2 **transition: Microstructure evolution, nanomechanical**
3 **behaviors and tensile properties**
4
5
6

7 Hong Wu^{a, *}, Yaojia Ren^a, Junye Ren^a, Luxin Liang^{a, **}, Ruidi Li^a, Qihong
8 Fang^b, Anhui Cai^c, Quan Shan^d, Yingtao Tian^e, Ian Baker^f
9
10
11

12
13 *^aState Key Laboratory of Powder Metallurgy, Central South University, Changsha*
14 *410083, PR China*
15
16

17
18 *^bState Key Laboratory of Advanced Design and Manufacturing for Vehicle Body,*
19 *Hunan University, Changsha 410082, PR China*
20
21

22
23 *^cCollege of Mechanical Engineering, Hunan Institute of Science and Technology,*
24 *Yueyang 414000, PR China*
25
26

27
28 *^dAcademy of Materials Science and Engineering, Kunming University of Science and*
29 *Technology, Kunming 650093, PR China*
30
31

32
33 *^eEngineering Department, Lancaster University, Lancaster LA1 4YW, United*
34 *Kingdom*
35
36

37
38 *^fThayer School of Engineering, Dartmouth College, Hanover NH 03755-8000, USA*
39
40

41
42 ** Corresponding author.*
43

44
45 *** Corresponding author.*
46
47

48
49 *E-mail addresses: hwucsu@csu.edu.cn (Hong Wu), liang_luxin@163.com (Luxin*
50 *Liang).*
51
52
53
54
55
56
57
58
59
60
61

Abstract

The effect of the volumetric energy density (*VED*) on the keyhole formation, microstructural evolution and associated mechanical properties of AlSi10Mg fabricated by selective laser melting (SLM) has been systematically investigated. The results indicated that three melting modes could be distinguished during the laser melting process, corresponding to different *VED* ranges, i.e. conduction mode ($<50 \text{ J mm}^{-3}$), transitional mode ($\sim 50\text{-}65 \text{ J mm}^{-3}$), and keyhole mode ($>65 \text{ J mm}^{-3}$). A high *VED* not only produced keyhole defects and hydrogen pores, but also generated two types of molten pool, i.e. a general shallow molten pool (GSP) and a keyhole-induced deep molten pool (KDP). The GSP was mainly consisted of an α -Al matrix, with $\sim 30 \mu\text{m}$ grains size, and enclosed by a $\sim 500 \text{ nm}$ eutectic Si cellular network. The grain size of the KDP was less than $15 \mu\text{m}$, and it has both a finer Si network ($\sim 200 \text{ nm}$) and nano-scale Si particles. No preferential crystallographic orientation could be observed within the KDP, while a strong texture along $\langle 111 \rangle$ orientation was exhibited in the GSP. These were responsible for the different mechanical properties of the SLM parts under different melting modes. The related mechanisms of the GSP and the KDP formation are comprehensively discussed and a correlation between the microstructure and the mechanical properties is also outlined.

Keywords: Selective laser melting; AlSi10Mg; melting mode; keyhole effect; mechanical properties

1. Introduction

Aluminum (Al) alloys, the second most widely used metallic structural material after steel, have broad potential for applications in aerospace, automotive, defense, and electronics [1, 2]. The performance of Al alloy parts produced by the traditional casting process is poor due to macro-segregation and the coarse structures resulted from the low cooling rates [3]. For the preparation of high-performance Al alloy parts, separate plastic processing (e.g. forging and extrusion) is no longer desirable, owing to the long production chain and limited flexibility [4]. Therefore, developing a new technology that can fabricate Al alloy parts in high quality and complex shapes has attracted extensive attention.

Additive manufacturing (AM) is a relatively new material processing method that interfuses computer-aided design with material processing and forming techniques [5]. Based on the principle of "discrete-superposition" and using stereolithography (STL) digital model files, functional and structural materials with complex geometries, high quality, and high dimensional precision can be prepared. This technology has the superiorities of high efficiency, high utilization rate of raw materials, and clean surface of all parts [6]. Selective laser melting (SLM) is the most adopted metal AM technology and has demonstrated the capability to manufacture functional parts with complex geometries and nearly full density from various pre-alloyed powders [7-9].

SLM of AlSi10Mg has been successfully commercialized and become the most popular one in applying additive manufacturing to Al alloys, owing to its low density, high specific strength, and ease of processing [10, 11]. The effect of SLM process parameters and post-treatment on its microstructure and mechanical properties has been extensively studied [12-14]. However, the investigation of microstructure evolution induced by the keyhole effect, i.e. vapor depression during melting, and its

relation to the mechanical behavior are very limited.

The keyhole effect, a notable phenomenon in laser welding, enables the generation of vapor capillaries (keyhole) via high laser energy [15]. The formation of these vapor capillaries elevates the energy absorption, resulting in the shape of molten pools changing from shallow to deep. Because of this stable full penetration process, keyhole mode laser welding has been widely used in industry [16, 17]. Recently, this common phenomenon was also noted in SLM due to the rapid development of high-power fiber lasers [18, 19]. For example, Aggarwal et al. [20] identified a transition from conduction to keyhole mode in SLM with increasing volumetric energy density (*VED*). In fact, the vaporization of materials is generally considered to be related to extra keyhole defects. To avoid this phenomenon, Cunningham et al. [21] determined the threshold of keyhole mode in SLM Ti-6Al-4V through ultrahigh-speed synchrotron X-ray imaging. Nevertheless, previous studies pointed out that pore-free parts with high mechanical properties (such as high strength, ductility, and wear resistance) can be obtained under keyhole mode [22-24]. However, the keyhole effect on the microstructure and mechanical properties of Al alloy (especially in AlSi10Mg) has rarely been reported. How the melt flows and eutectic Si phase changes during the SLM process remain unclear. Hence, this paper aims to obtain a comprehensive understanding of the solidification mechanisms, as well as the relationship between the microstructural evolution and mechanical properties at different melting modes.

In the present study, the effect of various *VEDs* on the transition of melting mode in SLM AlSi10Mg was investigated. The differences in the microstructure of the alloy under various melting modes have been analyzed. The associated mechanical properties, including nanoindentation hardness, creep behavior, and tensile strength were also studied.

2. Experimental Details

Spherical gas-atomized AlSi10Mg powders with an average particle size of 27 μm were utilized in this study. The AlSi10Mg specimens were prepared by a high-speed SLM machine (FS 271M, by Farsoon Inc., China) using a laser power (P) from 175-275 W and a scan speed (v) from 500-780 mm s^{-1} . The powder layer thickness (t) and the hatch spacing (h) were fixed at 50 μm , and 120 μm respectively. The integrated parameter VED was introduced as follows:

$$VED = \frac{P}{vth} \quad (1)$$

Therefore, the VED of specimens in this study ranged from 37 to 92 J mm^{-3} . The other conditions were described elsewhere and thus are not repeated here [25].

The microstructures of the SLM AlSi10Mg specimen were examined using an optical microscopy (OM, Leica DM-2700P) and a scanning electron microscope (SEM, FEI Nova NanoSEM 230) equipped with an electron backscatter diffraction (EBSD) apparatus. The top-view represents the building plane and the side-view represents the building direction plane. The deformation structures were carried out using a scanning transmission electron microscope (STEM, FEI Talos F200X 300 kV) imaging in both bright-field (BF) and high angle annular dark field (HAADF) modes. In addition, the density of the SLM AlSi10Mg part was measured by the Archimedes method (a theoretical density $\sim 2.68 \text{ g cm}^{-3}$ was used).

To evaluate the tensile strength at room temperature, flat dog-bone-shaped specimens were machined from the as-fabricated plates with gauge dimensions $8 \times 4 \times 2 \text{ mm}$. Tensile tests were performed by using an MTS machine (MTS systems, USA)

1 with a loading strain rate at $1 \times 10^{-3} \text{ s}^{-1}$. Nanoindentation tests were carried out using
2
3 a Nanoindenter (GSM) at room temperature. The maximum load was set at 30 mN
4
5
6 and the holding time was 15 s. Each indentation was repeated for five times in
7
8
9 adjacent region to eliminate any anomaly caused by the inhomogeneity of the material.
10
11 The nanoindentation creep experiments were performed at a constant load of 30 mN
12
13
14 by holding for 600 s after reaching the maximum load.
15

16 **3. Results**

17 **3.1 Effect of *VEDs* on densification and the melting mode**

18
19
20 As an essential index of the laser welding mode, *VED* is suitable for comprehensive
21
22 evaluation of SLM printing quality. Fig. 1 presents the relative density [25] of the
23
24 SLM specimens obtained at various *VEDs* and the corresponding metallographic
25
26 images of polished specimens. As the *VED* increased from 37 to 92 J mm^{-3} , the
27
28 relative density of the specimens decreased from $97.1 \pm 0.05\%$ to $95.2 \pm 0.15\%$. It is
29
30 worth noting that variations in process parameters (P , v) among the data points result
31
32 in variations in density at constant *VED*. Overall, the plot in Fig. 1 suggests that the
33
34 relative density tends to decrease with increasing *VED* in the given laser energy range,
35
36 which is in contrast to previous studies showing the relative density increases with
37
38 increasing *VED* [26]. This discrepancy is mainly ascribed to hydrogen pores and
39
40 keyhole defects generated by the increasing *VED*, as shown in the micrographs in Fig.
41
42 1a-i. Based on the recent work by Assuncao et al. [27], the melting mode of SLM can
43
44 be categorized into three types, i.e. conduction mode ($VED < 50 \text{ J mm}^{-3}$), transition
45
46 mode ($VED = 50\text{-}65 \text{ J mm}^{-3}$), and keyhole mode ($VED > 65 \text{ J mm}^{-3}$). The *VED*
47
48 applied in conduction mode is insufficient to stimulate substantial vaporization,
49
50 therefore, only a few gas pores can be observed on the metallographic images of
51
52
53
54
55
56
57
58
59
60
61
62
63
64
65

specimens (Fig. 1 a-c). When the *VED* is in the range of transition mode, the input energy becomes high enough to vaporize the metal, and thus induces a keyhole at the bottom of the molten pool. In addition to the large-scale (over 50 μm) hydrogen pores in metallographic images of specimens shown in Fig. 1 d-f, several gold-colored regions (referred to as keyhole-induced deep molten pool, KDP) were also observed inside the molten pool, as marked by arrows. As the *VED* is further increased into keyhole mode, the excessive input energy makes the vapor depression much higher than the surface tension. Therefore, the number of KDP, hydrogen pore, and keyhole defect increased significantly, as shown in metallographic images of the specimens (Fig. 1 g-i). By examining the side-view OM images (Fig. S1) of specimens “a”, “e” and “i” (from Fig. 1), it is evident that the shape of the molten pool changes significantly as the *VED* was varied. Compared to the general shallow molten pool (GSP) in Fig. S1a, the V-shaped KDP in side-view images is only observed in specimens under transition and keyhole modes. The keyhole effect is the prerequisite for the formation of the golden regions. Both the Gaussian distribution of laser energy and the short pause of the laser scanning could lead to the random distribution of KDP.

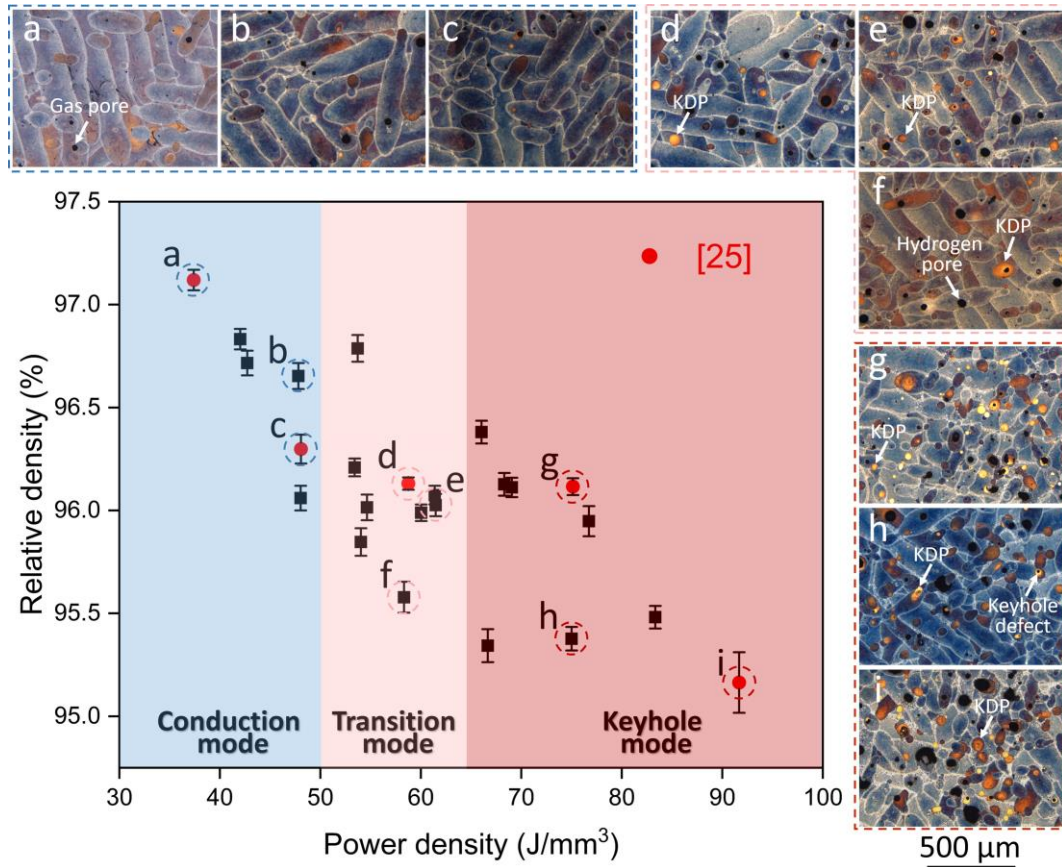


Fig. 1 Relationship between *VED* and relative density of the AlSi10Mg specimens fabricated by SLM, and the corresponding top-view metallographic images of the specimen labelled on the graph.

3.2 The Difference between the GSP and the KDP

To better understand the difference between the GSP and the KDP, SEM images at higher magnification of specimens “a” and “i” are shown in Fig. 2. The molten pool boundary of specimen “a” in top-view and side-view is shown in Fig. 2a. The molten track is characterized by novel eutectic cellular structures with a grey α -Al matrix enclosed by white Si networks. The side-view of the molten pools shows columnar α -Al grains surrounded by numerous elongated Si networks. During the SLM process, the chemical composition on both sides of the solid-liquid (S/L) interface is similar, and the columnar grains will grow along the maximal thermal dissipation direction

1 according to the heterogeneous nucleation and epitaxial growth mechanism [28].
2
3 Therefore, from the top-view and side-view SEM images, it can be inferred that the
4
5 three-dimensional structure of SLM AlSi10Mg is characterized by columnar primary
6
7 α -Al along the building direction surrounded by the intergranular eutectic Si network.
8
9 To better understand the structure of the cellular network, a deeply-etched specimen
10
11 was also examined in SEM, as shown in Fig. 2b. The top-view images of the
12
13 specimen show only the eutectic Si cellular network with a grid size of ~500 nm.
14
15
16
17
18
19

20 The KDP boundaries of specimen “i” in the top-view and side-view are also shown
21
22 in Fig. 2c. It is clear under high magnification in the SEM that the cells in the KDP
23
24 have a finer size than those in the surrounding GSP. This fine structure accounts for
25
26 the KDP region being gold-colored in the OM images. The KDP region presents a
27
28 light color when viewed under low magnification in the SEM. No keyhole defects
29
30 were observed at the bottom of this KDP, implying that the change in molten pool
31
32 shape does not necessarily result in keyhole defects. It shows that hydrogen pores are
33
34 the main reason for the decrease of density. The deeply etched KDP (Fig. 2d) exhibits
35
36 similar substructures compared to the conventional cellular network (Fig. 2b).
37
38 However, the size of the Si network (~200 nm, referred to as Si microtube) in the
39
40 KDP is much smaller than that in the GSP (~500 nm). Moreover, a large proportion of
41
42 the KDP does not have the microtube structure owing to the strong convection of the
43
44 melt flow, which means that the nano-scale Si particles (as marked in Fig. 2d) are
45
46 unevenly distributed.
47
48
49
50
51
52
53
54
55
56
57
58
59
60
61
62
63
64
65

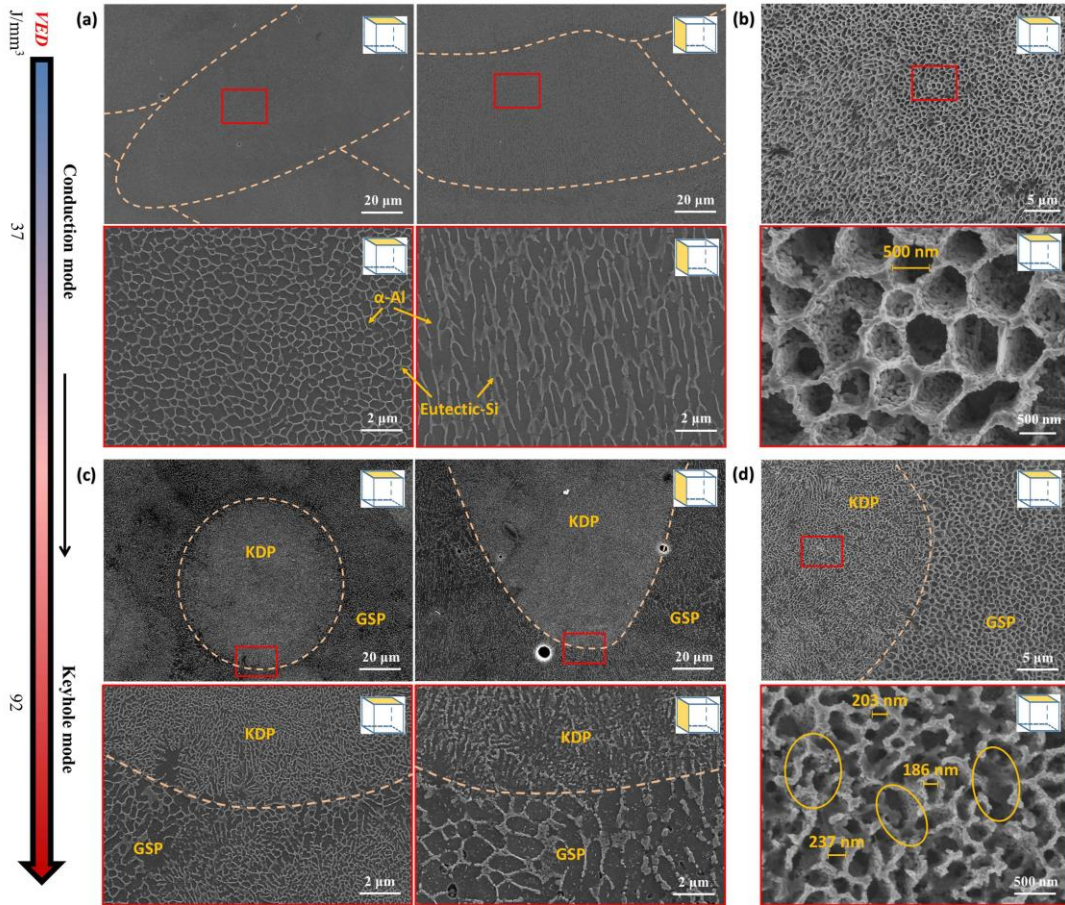


Fig. 2 SEM microstructures from top-view and side-view of the GSP and the KDP under (a) conduction and (c) keyhole mode; the top-view of (b) GSP and (d) KDP structures after deep etching.

3.3 EBSD and Texture Analysis

The EBSD results from the KDP obtained from the side-view of specimen “i” are displayed in Fig. 3. In order to determine the grain size distribution and grain boundary misorientations, the boundaries between the KDP and the GSP are delineated in Fig. 3a (lines inside the box). A bimodal grain size distribution was found in the side-view images (Fig. 3b), consisting of fine and coarse groups. To compare the grain sizes in different regions, we selected sections inside the box with grain sizes either higher than 20 μm or less than 15 μm , and the results are shown in the corresponding poles figures (PF) in Fig. 3c and 3d. It is illustrated that the grain

size around the GSP is larger than 20 μm and a strong $\langle 111 \rangle$ texture is observed. In the KDP, the grain size is less than 15 μm and the orientation of the grains is irregular owing to the fluctuations of the heat flow and multiple remelting. In addition, the grain sizes in both the GSP and the KDP are an order of magnitude larger than those of Si networks, revealing that the cells are subgrains.

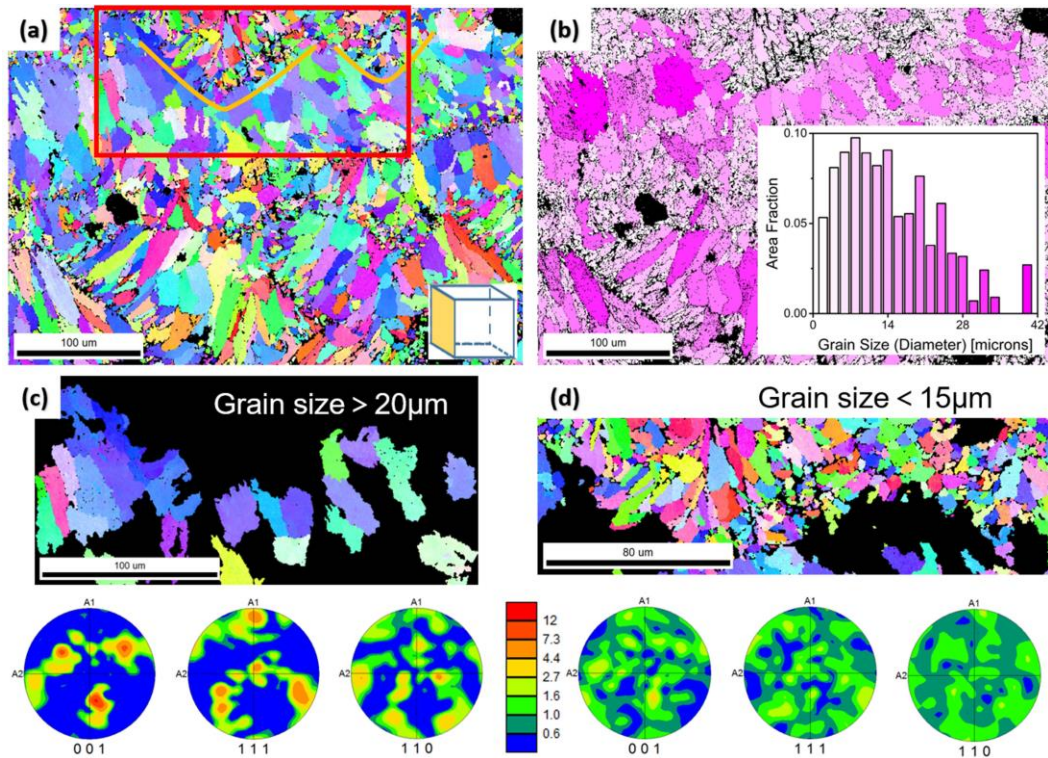


Fig. 3 EBSD analysis of the KDP: (a) Inverse pole figure images; (b) the distribution of grain sizes; (c) the region with grain size larger than 20 μm and corresponding pole figures; and (d) the region with grain size less than 15 μm and corresponding pole figures.

3.4 Nanoindentation

Nanoindentation hardness and creep tests were performed on the KDP and the GSP of transverse (T) and longitudinal (L) sections of specimen “i”. Fig. 4a shows load-displacement curves of the GSP-T, the KDP-T, the GSP-L, and the KDP-L under a load of 30 mN. The hardness of corresponding indents is calculated, as shown in Fig.

1 4b. The hardness of the KDP in the SLM specimen is apparently higher than that of
2
3 the GSP, and the hardness in the longitudinal section is higher than that in the
4
5 transverse section for the same molten pool. Typical depth-time curves are shown in
6
7 Fig. 4c. The displacement curves initially show a linear relationship, but eventually
8
9 reach a stable state at longer time. By determining the stress exponent of the material,
10
11 it is possible to illustrate the creep mechanism. The power-law relation [29] for strain
12
13 rate during nanoindentation creep can be written:

$$\dot{\epsilon} = C \sigma^n \quad (2)$$

22 in which C is a constant, σ refers to the applied stress on the material, and n denotes
23
24 the stress exponent. The stress σ can be defined as the applied load P divided by the
25
26 contact area A_C in the uniaxial tensile test. The stress state under the nanoindentation
27
28 is complicated. For a Berkovich indenter, A_C can be approximated as $A_C = 24.5h^2$,
29
30 where h is the displacement of the indenter [30]. Because the shape of the indentation
31
32 formed during creep is indicative of the indenter depth, the indentation strain rate $\dot{\epsilon}$
33
34 can be replaced by the ratio of the instantaneous rate h' and the head displacement h ,
35
36 where the instantaneous rate h' is the first derivative of the head displacement h versus
37
38 time t [31]. Fig. 4d presents the corresponding strain rate versus stress curves. The
39
40 stress exponents of the GSP-T, the GSP-L, the KDP-T, and the KDP-L specimens are
41
42 52, 32, 28, and 23, respectively. It is obvious that the stress exponents of the GSP are
43
44 higher than those of the KDP, and anisotropy is evident by comparing the data in the
45
46 transverse and longitudinal sections. Such high-stress exponents for SLM AlSi10Mg
47
48 have not been reported in other cast alloys.
49
50
51
52
53
54
55
56
57
58
59
60
61
62
63
64
65

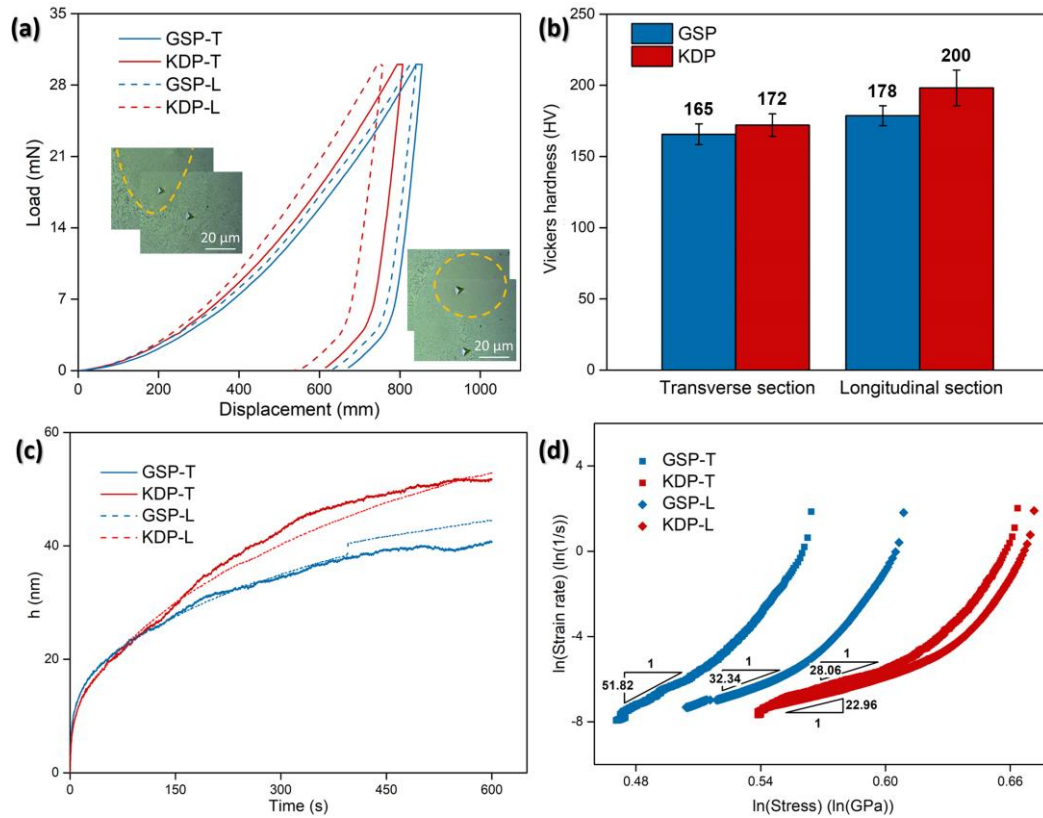


Fig. 4 Nanoindentation measurements of the KDP and the GSP: (a) load-displacement curves, (b) hardness; (c) displacement-time curves under a load of 30 mN at room temperature; (d) ln-ln plots of strain rate versus stress.

3.5 Tensile properties

Figure 5 shows the tensile properties of SLM AlSi10Mg specimens with various *VEDs* (from 37 to 92 J/mm³) [25]. Obviously, the ultimate tensile strength (UTS) of SLM specimens still maintains a high level (~450 MPa) at transition mode, and only decreases as *VED* further increases to keyhole mode. By contrast, the clear downward trend of yield strength (YS) appears earlier (~58 J mm⁻³), as marked in Fig 5. Porosity is one of the main factors affecting tensile properties. The growing pores will reduce the actual load-bearing portion of the section and degrade the tensile properties. Looking back on the change of density, it can be inferred that the tensile properties did not immediately decrease as expected owing to the formation of KDP. In addition,

1 the elongation (EL) presents a trend of first increasing and then decreasing, and
 2
 3 reaches the maximum value of $7.7 \pm 2.1\%$ at the transition mode. For comparison, the
 4
 5 tensile test is performed on as-cast specimens. The corresponding true stress and
 6
 7 work-hardening rate ($\theta = d\sigma/d\varepsilon$) versus true strain curves of SLM and as-cast
 8
 9 specimens are shown in Fig. S2. It is clear that the work-hardening rate of the SLM
 10
 11 specimen is still very high (~ 2000 MPa) up to fracture. While the work-hardening rate
 12
 13 of the as-cast specimen is lower and drops rapidly, with the necking stage occurring at
 14
 15 the strain of 0.087. The values of tensile properties, such as ultimate tensile strength
 16
 17 (UTS), yield strength (YS), and elongation (EL) in this study are summarized in Table
 18
 19
 20
 21
 22
 23
 24
 25
 26 S1.

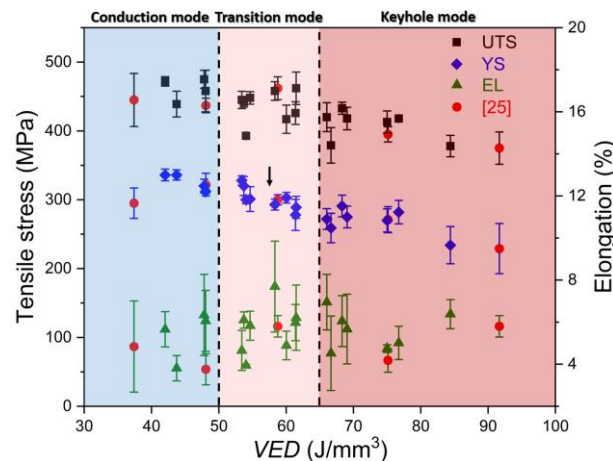


Fig. 5 Tensile properties of SLM AlSi10Mg specimens for various VEDs [25].

48 Figure 6 shows fractographs of SLM AlSi10Mg specimens processed at various
 49 VEDs as well as the as-cast alloy at different magnifications. It is evident that both the
 50 size and number of pores increase with increasing VED. A large number of dimples
 51 without pores can be observed in the fractograph of the as-cast specimen, indicating
 52 the occurrence of substantial plastic deformation during the tensile testing. In contrast,
 53
 54
 55
 56
 57
 58
 59
 60
 61
 62
 63
 64
 65

the fractographs of SLM specimens exhibit typical brittle cleavage fracture, which is responsible for the low ductility. Interestingly, the morphology of the cleavage plane is similar to that of the Si network, indicating that the high strength and relatively low elongation of SLM specimens are related to the eutectic Si networks.

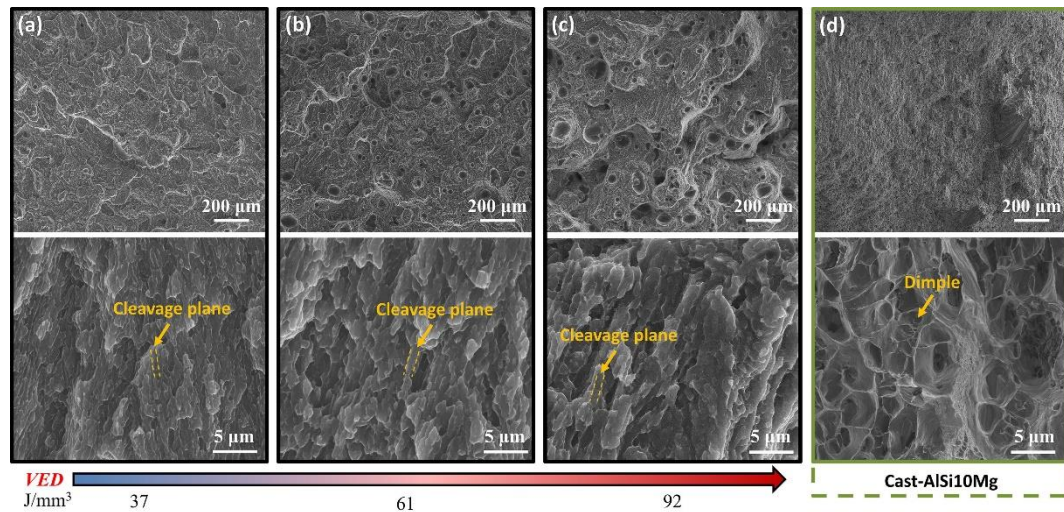
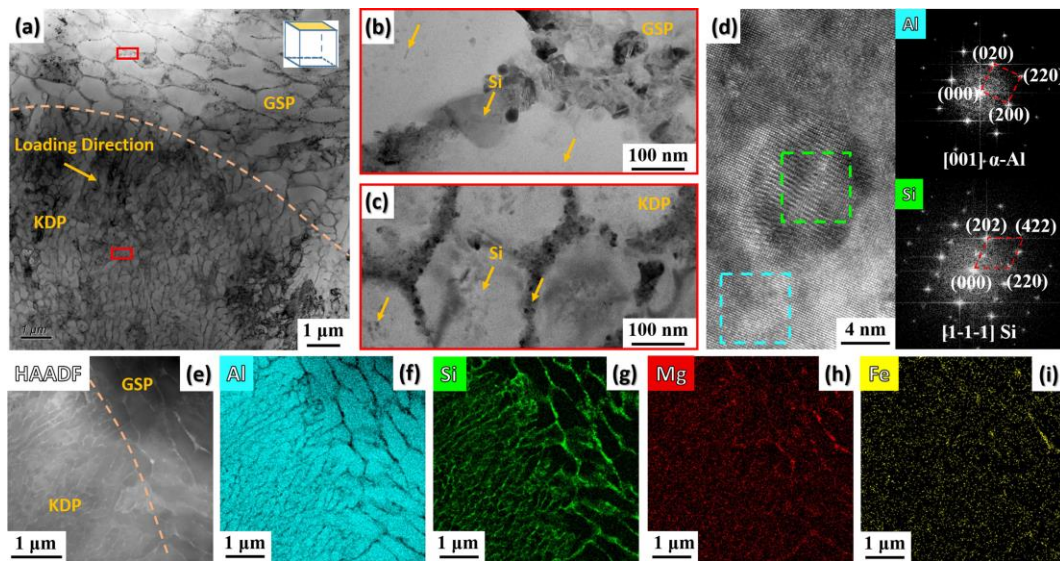


Fig. 6 Fractographs of SLM specimens (a) specimen “a”, (b) specimen “e”, (c) specimen “i” and (d) as-cast specimen.

3.6 TEM analysis

To further verify the contribution of the KDP in deformation, a typical bright field (BF) STEM top-view image of SLM AlSi10Mg (specimen “i”) after tensile testing is shown in Fig. 7a. Although the cells in both the GSP and the KDP show evidence of deformation after tensile testing, the KDP still consisted of a high density of finer cells (~200 nm, a similar size to undeformed cells), indicating much lower deformation than the GSP (the size of Si network is more than 1 μm along loading direction). Note that the width of the cell boundaries in the GSP is slightly larger than that in the KDP (Fig. 7b and c). In addition, a few Si precipitates are observed inside both cells, see Fig. 7b and c, with no obvious difference between them. An HRTEM

1 image of a typical Si precipitate along with fast Fourier transforms (FFT) of the
 2 Al-matrix and Si precipitate are shown in Fig. 7d. The FFTs indicate an orientation
 3 relationship of $([001]_{\text{Al}}/[1-1-1]_{\text{Si}}$ and $(020)_{\text{Al}}//((202)_{\text{Si}})$ between the α -Al matrix and
 4 the precipitate. The streaking in FFTs indicates that stacking faults exist in the Si
 5 precipitates. Fig. 7e-i present the HAADF-STEM image and corresponding energy
 6 dispersive X-ray (EDS) maps of the cells. The elemental mapping clearly shows that
 7 the elongated cell boundaries contain a Si phase, which is consistent with the SEM
 8 results (Fig. 2). Additionally, segregation of the Mg and Fe only occurs at cell
 9 boundaries/triple junctions of the GSP (Fig. 7h-i).



44 Fig. 7 TEM BF image of (a) low and (b-c) high magnification (corresponding to the
 45 red regions indicated in Fig. 7a) showing the elongated cellular-like structure
 46 observed in SLM AlSi10Mg specimen “i” after tensile testing; (d) HRTEM image of
 47 a Si precipitate along with the FFTs; (e-i) HAADF-STEM image and corresponding
 48 EDS maps of Al, Si, Mg and Fe elements.

54 4. Discussion

57 4.1. Microstructural evolution

1 The distinctive SLM forming process is essentially solidification and accumulation
2
3 of micro molten pools in different regions. It is well accepted that superheating during
4
5 the SLM process leads to an inhomogeneous microstructure (10-200 nm Al-rich and
6
7 Si-rich regions) of the molten pool in Al-Si based alloys [14, 32]. In the subsequent
8
9 solidification process, the α -Al phase first precipitates and grows from the liquid
10
11 phase, thereby enhancing the concentration of Si-rich regions in the residual liquid.
12
13 This makes it enter the eutectic region, resulting in eutectic phase evolution by the
14
15 co-operative growth of two phases [33, 34]. This sequential solidification of
16
17 AlSi10Mg will produce a two-phase distribution of α -Al and eutectic Si. Due to the
18
19 low cooling rate in conventional castings, the eutectic Si particles grow and
20
21 eventually form large rods or needles [35]. However, the large temperature gradient in
22
23 SLM induces a high degree of undercooling and high surface tension gradient, hence
24
25 leading to Marangoni flow in different convection modes. Initially, a novel
26
27 well-ordered structure forms by both diffusion and transportation via
28
29 Bénard-Marangoni drifting convection (Fig. 8). Subsequently, cellular subgrains were
30
31 nucleated at the high cooling rate, which gives rise to the formation of a
32
33 super-saturated Al matrix containing a fine Si network in the SLM AlSi10Mg.
34
35
36
37
38
39
40
41
42
43
44
45
46
47
48
49
50
51
52
53
54
55
56
57
58
59
60
61
62
63
64
65

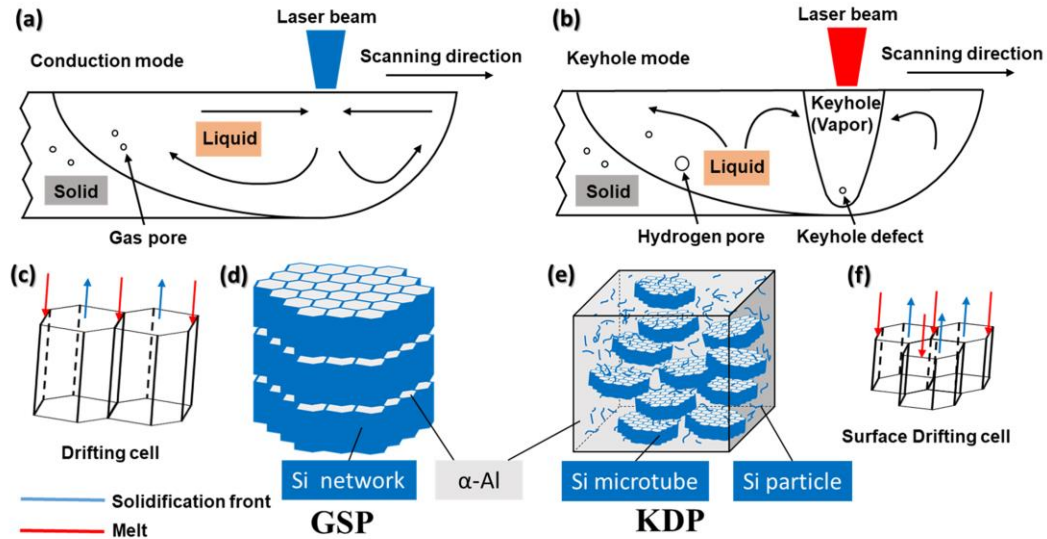


Fig. 8 Schematic diagram of (a) conduction mode and (b) keyhole mode, (c) drifting cell and (f) surface drifting cell, (d) the GSP and (e) the KDP microstructures.

4.2 The formation mechanism of KDP

The formation of the KDP is commonly accompanied by keyhole defects, i.e. pores inside the gold-colored regions [24]. However, compared with the conduction mode, the keyhole mode has the advantages of both a small melting zone and a small heat-affected zone, thereby reducing the occurrence of cracks [22, 36]. A high *VED* is conducive to instantly melting and evaporating the alloy, and thus forming a keyhole, as shown in Fig. 8b. The formation of a stable V-shaped keyhole is attributed to the balance between the recoil pressure and surface tension. Once the laser is removed, the metal liquid in the molten pool will backfill into the keyhole owing to the high surface tension and the hydrostatic pressure [37]. If the backfilling is insufficient, the keyhole defects form at the bottom of the deep molten pool. Otherwise, the KDP with a fine microstructure will be produced. There are two major reasons for the formation of the fine substructures in the KDP. On one hand, at higher *VEDs*, the elevated

1 temperature gradient makes the internal convection of the molten pool transit from
2
3 Drifting Cell (DC) to Surface Drifting Cell (SDC) mode [38]. The SDC mode has a
4
5 smaller convection size and more intense convection level. Fine Si microtubes
6
7 (<200 nm) are subsequently generated at high cooling rates. On the other hand, there
8
9 is strong turbulence in the KDP arising from melt backfill, which prevents the
10
11 formation of a continuous Si network. The unevenly distributed nano-scale Si
12
13 particles are deposited in the solidified microstructure.
14
15
16
17
18
19

20 4.3 Mechanical properties analysis 21

22 Based on the aforementioned analysis, the GSP region consists of an α -Al matrix
23
24 combined with a eutectic Si cellular network in a specific direction (Fig. 8d), while
25
26 the KDP region consists mainly of an α -Al matrix, Si microtubes, and nano-scale Si
27
28 particles (Fig. 8e). The nanoindentation hardness is significantly dependent on the
29
30 ratio of the α -Al volume fraction to that of the eutectic Si in the contact area between
31
32 the indenter and the specimen. Since the microhardness of the Si phase (≈ 950 HV) is
33
34 much higher than that of the α -Al phase (≈ 70 HV) [39, 40], increasing the fraction of
35
36 the Si phase in the eutectic structure can greatly increase the hardness of the alloy.
37
38 The creep mechanisms of metal materials are mainly determined by diffusion and the
39
40 motion of dislocations [41]. It is well accepted that the stress exponent is a useful
41
42 indicator to infer the creep mechanism. For example, $n = 1$ for diffusion creep, $n \approx 2$
43
44 for grain boundary sliding, $3 < n < 6$ for a dislocation-climb mechanism, and $7 < n <$
45
46 10 for a dislocation slip mechanism [42-44]. Particularly, in the case of extremely
47
48 high-stress exponents ($n > 10$), the creep mechanism is generally considered to
49
50
51
52
53
54
55
56
57
58
59
60
61
62
63
64
65

1 involve a high-density of dislocation-particle interactions [45]. This phenomenon
2
3 usually occurs in multi-component or multi-phase engineering alloys, such as Al
4
5 metal matrix composites (MMCs). Therefore, SLM AlSi10Mg specimens can be
6
7 considered as MMCs where nano-sized eutectic Si networks act as “reinforcement
8
9 particles” [46]. The dislocations motion in the GSP was pinned by the eutectic Si
10
11 networks, resulting in an abnormally high creep stress exponent. However, some of
12
13 the Al matrix remains interconnected in the KDP, which allows dislocations to bypass
14
15 the “reinforcement particles”, thereby alleviating the dislocation-particle interactions
16
17 and reducing the stress exponents. Moreover, the refined grain size in the KDP could
18
19 increase the grain boundary activity, which also reduces the stress exponents [47]. As
20
21 previously reported in SLM IN738LC alloys, the anisotropy of creep behavior in the
22
23 SLM specimens is attributed to the columnar grains and Si networks growing along
24
25 the building direction [48]. The lower stress exponents on longitudinal sections arise
26
27 because the grain and cell boundaries parallel to building direction have been mostly
28
29 eliminated. Compared to the creep tests on the GSP, the columnar-free microstructure
30
31 in the KDP can effectively alleviate creep anisotropy.
32
33
34
35
36
37
38
39
40
41
42
43
44

45 Turning to the tensile properties, although the supersaturated Al matrix and Si
46
47 precipitates are the reasons for the enhancements of the strength, the anomalous
48
49 hardening capacity is the main contributing factor in strengthening of SLM specimens
50
51 as compared with those of as-cast specimens. However, the strength enhancements
52
53 come at the cost of decreased elongation, i.e. severe deformation and even cracking
54
55 along the Si networks (Fig. S3) during deformation, and sudden fracture after
56
57
58
59
60
61
62
63
64
65

1 reaching the ultimate tensile stress without any necking. This anomalous
2
3 work-hardening capacity, as presented in Fig. S2, has been shown to be related to the
4
5 Si networks [49]. During tensile plastic deformation, the hard-phase Si network
6
7 restricts the deformation of the soft-phase Al matrix near the interfaces, therefore
8
9 generating large strain gradients and a high density of geometrically necessary
10
11 dislocations at the Al/Si interface. The KDP with interconnected Al matrix and Si
12
13 microtubes effectively released the strain gradient at the interface, thus reducing the
14
15 possibility of local cracks and significantly improving the elongation. Wu et al. [50]
16
17 have suggested that dislocations are transmitted through the thin Si network
18
19 boundaries during deformation, which means that dislocations are more likely to glide
20
21 through the KDP structure. Furthermore, the extra characteristics of the KDP, such as
22
23 small grain size, high solid solubility, and no preferred orientation, could also
24
25 effectively improve mechanical properties and alleviate anisotropic behavior. The
26
27 ultimate tensile stress and elongation of the SLM and as-cast Al-Si alloys in this work
28
29 are compared with values in the literature [14, 32, 51-61], as shown in Fig. 9. With an
30
31 excellent combination of strength and ductility, the mechanical performance of SLM
32
33 AlSi10Mg alloy in this study exceeds the previously reported SLM Al-Si alloys,
34
35 making it a promising candidate for practical applications. Besides, it is worth noting
36
37 that the tensile properties of SLM specimens are generally superior to as-cast alloys,
38
39 which indicates that SLM, as an emerging technology, has a great potential to fill gaps
40
41 in traditional technologies.
42
43
44
45
46
47
48
49
50
51
52
53
54
55
56
57
58
59
60
61
62
63
64
65

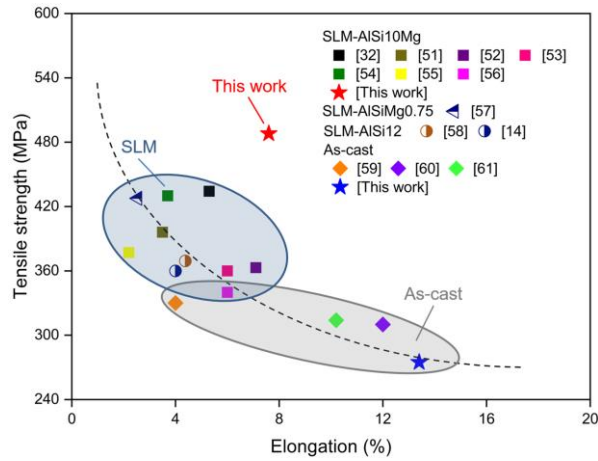


Fig. 9 Plot of tensile stress versus elongation for various Al-Si alloys, including both the current work and data from the literature.

However, the balance between the KDP and pores has become a new issue. The specimens under keyhole mode have the most KDPs, but high density of accompanying pores limits the improvement of mechanical properties of the alloy. By drying the raw powder at high-temperature, the hydrogen pores (the main part of the defects) formed by the reaction between aluminum and H₂O can be avoided [25], which provides an exciting prospect for solving this problem. Thus, the KDP formed by the keyhole effect might offer the possibility of overcoming the strength-ductility trade-off for Al-Si alloys. A thorough study of SLM AlSi10Mg with full-KDP and high density will be reported in future publications.

5. Conclusions

In this work, the solidification mechanisms, microstructural evolution, and mechanical properties of AlSi10Mg fabricated by SLM at different *VEDs* have been systematically studied. Based on these experimental results and analysis, the following conclusions can be drawn:

- 1 (1) Three types of melting mode, i.e. conduction mode, transition mode, and keyhole
2
3 mode, occur in SLM AlSi10Mg, which are strongly dependent on the *VED*. The
4
5 relative density decreases with increasing *VED* owing to the elevated
6
7 concentration of hydrogen pores and keyhole defects upon the transition from
8
9 conduction mode to keyhole mode.
10
11
12
13
14 (2) The SLM AlSi10Mg, consisting mainly of eutectic Si and α -Al phases, exhibits
15
16 two archetypal molten pools, i.e. the GSP and the KDP. The GSP structures have
17
18 $\sim 30 \mu\text{m}$ grains with $\langle 111 \rangle$ strong texture and contain a $\sim 500 \text{ nm}$ eutectic Si
19
20 cellular network. The grain size in the KDP is less than $15 \mu\text{m}$ without any
21
22 preferred orientation. The KDP substructures include $\sim 200 \text{ nm}$ eutectic Si
23
24 microtubes and nano-scale Si particles.
25
26
27
28
29
30
31 (3) The nanoindentation hardness of the AlSi10Mg specimens fabricated under the
32
33 keyhole mode is 165-200 HV. Owing to the finer subgrains, the nanoindentation
34
35 hardness is higher in the KDP than the GSP. The different microstructures
36
37 observed in transverse and longitudinal sections are also revealed in the
38
39 anisotropy of the nanoindentation hardness values.
40
41
42
43
44 (4) The high-stress exponents of the SLM AlSi10Mg indicate that the creep behavior
45
46 is controlled by a high-density of dislocation-particle interactions. The
47
48 columnar-free microstructure in the KDP can effectively alleviate the anisotropy
49
50 of the creep behavior.
51
52
53
54
55 (5) The UTS of SLM specimens in current study is more than 70% higher than those
56
57 of as-cast specimens, with an acceptable sacrifice of ductility. The SLM
58
59
60
61
62
63
64
65

1 AlSi10Mg fabricated in the transition mode at a *VED* of 58 J mm⁻³ exhibits a high
2
3 tensile strength (UTS: 458 ± 13.6 MPa, YS: 293 ± 8.0 MPa) combined
4
5
6 with reasonable ductility (7.7 ± 2.1%).
7
8
9

10 **Acknowledgments**

11
12 The research was supported by the National Key Research and Development Program of
13
14 China (No. 2016YFB1100103), National Natural Science Foundation of China (No.
15
16 51771233), and Fundamental Research Funds for the Central Universities of Central South
17
18 University (No. 2018ZZTS127). The authors would thank the support of collaboration from
19
20 The Royal Society through International Exchanges 2018 Cost Share (China) scheme (No.
21
22 IEC\NSFC\181278). The authors would also thank Sinoma Institute of Materials Research
23
24 (Guang Zhou) Co., Ltd. for the assistance in TEM characterization.
25
26
27
28
29
30
31
32
33
34
35
36
37
38
39
40
41
42
43
44
45
46
47
48
49
50
51
52
53
54
55
56
57
58
59
60
61
62
63
64
65

References

- [1] H.B. Yang, M.N. Li, H.Y. Bu, X. Lu, Effects of alloying elements on the amounts of $MgZn_2$ and S-Al₂CuMg phase in 7075 aluminum alloy, *Journal of Micromechanics and Molecular Physics*, (2020) 2050003.
- [2] S.L. Cai, J.C. Wan, Y.J. Hao, C.C. Koch, Dual gradient microstructure to simultaneously improve strength and electrical conductivity of aluminum wire, *Materials Science and Engineering A*, 783 (2020) 139308.
- [3] M.F. Hafiz, T. Kobayashi, A study on the microstructure-fracture behavior relations in Al-Si casting alloys, 30 (1994) 475-480.
- [4] K. Wu, K. Deng, K. Nie, Y. Wu, X. Wang, X. Hu, M. Zheng, Microstructure and mechanical properties of SiCp/AZ91 composite deformed through a combination of forging and extrusion process, *Materials & Design*, 31 (2010) 3929-3932.
- [5] J. Liu, E. Stevens, Q. Yang, M. Chmielus, A.C. To, An analytical model of the melt pool and single track in coaxial laser direct metal deposition (LDMD) additive manufacturing, *Journal of Micromechanics and Molecular Physics*, (2017) 1750013.
- [6] C. Han, B. Rita, J.C.D. Qiu, U. Ramamurty, K. Zhou, Microstructure and mechanical properties of (TiB+TiC)/Ti composites fabricated in situ via selective laser melting of Ti and B4C powders, *Additive Manufacturing*, (2020) 101466.
- [7] T. Long, X. Zhang, Q. Huang, L. Liu, Y. Liu, J. Ren, Y. Yin, D. Wu, H. Wu, Novel Mg-based alloys by selective laser melting for biomedical applications: microstructure evolution, microhardness and in vitro degradation behaviour, *Virtual and Physical Prototyping*, 13 (2018) 71-81.
- [8] Y. Yin, Q. Huang, L. Liang, X. Hu, T. Liu, Y. Weng, T. Long, Y. Liu, Q. Li, S. Zhou, In vitro degradation behavior and cytocompatibility of ZK30/bioactive glass composites fabricated by selective laser melting for biomedical applications, *Journal of Alloys and Compounds*, 785 (2019) 38-45.
- [9] H. Wu, L. Liang, H. Zeng, X. Lan, W. Huang, Microstructure and nanomechanical properties of Zr-based bulk metallic glass composites fabricated by laser rapid prototyping, *Materials Science and Engineering A*, 765 (2019) 138306.
- [10] N.T. Aboulkhair, M. Simonelli, L. Parry, I. Ashcroft, C. Tuck, R. Hague, 3D printing of Aluminium alloys: Additive Manufacturing of Aluminium alloys using selective laser melting, *Progress in Materials Science*, 106 (2019) 100578.
- [11] L. Thijs, K. Kempen, J. P. Kruth, J. Van Humbeeck, Fine-structured aluminium products with controllable texture by selective laser melting of pre-alloyed AlSi10Mg powder, *Acta Materialia*, 61 (2013) 1809-1819.
- [12] Y. Ren, L. Liang, Q. Shan, A. Cai, J. Du, Q. Huang, S. Liu, X. Yang, Y. Tian, H. Wu, Effect of volumetric energy density on microstructure and tribological properties of FeCoNiCuAl high-entropy alloy produced by laser powder bed fusion, 15(S1) (2020) 543-554.
- [13] L. Zhou, T. Yuan, R. Li, J. Tang, M. Wang, F. Mei, Microstructure and mechanical properties of selective laser melted biomaterial Ti-13Nb-13Zr compared to hot-forging, *Materials Science & Engineering A*, 725 (2018) 329-340.
- [14] X. Li, X. Wang, M. Saunders, A. Suvorova, L. Zhang, Y. Liu, M. Fang, Z. Huang, T.B. Sercombe, A selective laser melting and solution heat treatment refined Al-12Si alloy with a controllable ultrafine eutectic microstructure and 25% tensile ductility, *Acta Materialia*, 95 (2015) 74-82.
- [15] H. Zhao, T. Debroy, Macroporosity free aluminum alloy weldments through numerical simulation of keyhole mode laser welding, *Journal of Applied Physics*, 93 (2003) 10089-10096.

- 1 [16] W. Huang, H. Wang, T. Rinker, W. Tan, Investigation of metal mixing in laser keyhole welding of
2 dissimilar metals, *Materials & Design*, 195 (2020) 109056.
- 3 [17] J. Ning, L.J. Zhang, L.L. Zhang, J. Long, X.Q. Yin, J.X. Zhang, S. J. Na, Effects of power
4 modulation on behaviours of molten pool and keyhole during laser-arc hybrid welding of pure copper,
5 *Materials & Design*, (2020) 108829.
- 6 [18] J. Dilip, S. Zhang, C. Teng, K. Zeng, C. Robinson, D. Pal, B. Stucker, Influence of processing
7 parameters on the evolution of melt pool, porosity, and microstructures in Ti-6Al-4V alloy parts
8 fabricated by selective laser melting, *Progress in Additive Manufacturing*, 2 (2017) 157-167.
- 9 [19] T. Guraya, S. Singamneni, Z. Chen, Microstructure formed during selective laser melting of
10 IN738LC in keyhole mode, *Journal of Alloys and Compounds*, 792 (2019) 151-160.
- 11 [20] A. Aggarwal, S. Patel, A. Kumar, Selective Laser Melting of 316L Stainless Steel: Physics of
12 Melting Mode Transition and Its Influence on Microstructural and Mechanical Behavior, *Jom*, (2018).
- 13 [21] R. Cunningham, C. Zhao, N. Parab, C. Kantzos, J. Pauza, K. Fezzaa, T. Sun, A.D. Rollett,
14 Keyhole threshold and morphology in laser melting revealed by ultrahigh-speed x-ray imaging,
15 *Science*, 363 (2019) 849-852.
- 16 [22] T. Qi, H. Zhu, H. Zhang, J. Yin, L. Ke, X. Zeng, Selective laser melting of Al7050 powder:
17 Melting mode transition and comparison of the characteristics between the keyhole and conduction
18 mode, *Materials & Design*, 135 (2017) 257-266.
- 19 [23] J. Yang, J. Han, H. Yu, J. Yin, M. Gao, Z. Wang, X. Zeng, Role of molten pool mode on
20 formability, microstructure and mechanical properties of selective laser melted Ti-6Al-4V alloy,
21 *Materials & Design*, 110 (2016) 558-570.
- 22 [24] H. Wu, Y. Ren, J. Ren, A. Cai, M. Song, Y. Liu, X. Wu, Q. Li, W. Huang, X. Wang, Effect of
23 melting modes on microstructure and tribological properties of selective laser melted AlSi10Mg alloy,
24 *Virtual and Physical Prototyping*, 15(S1) (2020) 570-582.
- 25 [25] H. Wu, J. Ren, Q. Huang, X. Zai, L. Liu, C. Chen, S. Liu, X. Yang, R. Li, Effect of laser
26 parameters on microstructure, metallurgical defects and property of AlSi10Mg printed by selective
27 laser melting, *Journal of Micromechanics & Molecular Physics*, 02 (2017) 1750017.
- 28 [26] A.H. Maamoun, Y.F. Xue, M.A. Elbestawi, S.C. Veldhuis, Effect of SLM Process Parameters on
29 the Quality of Al Alloy Parts; Part I: Powder Characterization, Density, Surface Roughness, and
30 Dimensional Accuracy, *Materials*, (2018) 2343.
- 31 [27] E. Assuncao, S. Williams, D. Yapp, Interaction time and beam diameter effects on the conduction
32 mode limit, *Optics and Lasers in Engineering*, 50 (2012) 823-828.
- 33 [28] M. Rappaz, S. David, J. Vitek, L. Boatner, Development of microstructures in Fe-15Ni-15Cr
34 single crystal electron beam welds, *Metallurgical Transactions A*, 20 (1989) 1125-1138.
- 35 [29] R. Goodall, T. Clyne, A critical appraisal of the extraction of creep parameters from
36 nanoindentation data obtained at room temperature, *Acta materialia*, 54 (2006) 5489-5499.
- 37 [30] C.C. Huang, M. K. Wei, S. Lee, Transient and steady-state nanoindentation creep of polymeric
38 materials, *International Journal of Plasticity*, 27 (2011) 1093-1102.
- 39 [31] J. Campbell, J. Dean, T.W. Clyne, Limit Case Analysis of the "Stable Indenter Velocity" Method
40 for Obtaining Creep Stress Exponents from Constant Load Indentation Tests, *Mechanics of
41 Time-Dependent Materials*, 21 (2015) 1-13.
- 42 [32] W. Li, S. Li, J. Liu, A. Zhang, Y. Zhou, Q. Wei, C. Yan, Y. Shi, Effect of heat treatment on
43 AlSi10Mg alloy fabricated by selective laser melting: Microstructure evolution, mechanical properties
44 and fracture mechanism, *Materials Science and Engineering: A*, 663 (2016) 116-125.
- 45
46
47
48
49
50
51
52
53
54
55
56
57
58
59
60
61
62
63
64
65

- [33] M.C. Flemings, Solidification processing, Metallurgical Transactions, 5 (1974) 2121-2134.
- [34] Y.T. Pei, J.T.M.D. Hosson, Functionally graded materials produced by laser cladding, Acta Materialia, 48 (2000) 2617-2624.
- [35] J. Suryawanshi, K.G. Prashanth, S. Scudino, J. Eckert, O. Prakash, U. Ramamurty, Simultaneous enhancements of strength and toughness in an Al-12Si alloy synthesized using selective laser melting, Acta Materialia, 115 (2016) 285-294.
- [36] M. Kutsuna, K. Shido, T. Okada, Fan-shaped cracking test of aluminum alloys in laser welding, Proceedings of SPIE - The International Society for Optical Engineering, 4831 (2003) 230-234.
- [37] D. Zhang, M. Wang, C. Shu, Y. Zhang, D. Wu, Y. Ye, Dynamic keyhole behavior and keyhole instability in high power fiber laser welding of stainless steel, Optics & Laser Technology, 114 (2019) 1-9.
- [38] A.I. Mizev, D. Schwabe, Convective instabilities in liquid layers with free upper surface under the action of an inclined temperature gradient, Physics of Fluids, 21 (2009) 112102.
- [39] S.T. Islam, P. Das, S. Das, Deformation behaviour of Rheocast A356 Al alloy at microlevel considering approximated RVEs, Metals & Materials International, 21 (2015) 311-323.
- [40] Y. Zhang, T. Gao, X. Liu, Influence of Ge content on the microstructure, phase formation and microhardness of hypereutectic Al-Si alloys, Journal of Alloys & Compounds, 585 (2014) 442-447.
- [41] S. Spigarelli, R. Sandström, Basic creep modelling of aluminium, Materials Science and Engineering: A, 711 (2018) 343-349.
- [42] Xiaoyan, Liu, Qianqian, Zhang, Xicheng, Zhao, Xirong, Yang, Lei, Luo, Ambient-temperature nanoindentation creep in ultrafine-grained titanium processed by ECAP, Materials Science & Engineering A, 676 (2016) 73-79.
- [43] M.A.E. Jepson, Investigation of short-term creep deformation mechanisms in MarBN steel at elevated temperatures, Materials Science & Engineering A, 734 (2018) 491-505.
- [44] H. Dieringa, N. Hort, K.U. Kainer, Investigation of minimum creep rates and stress exponents calculated from tensile and compressive creep data of magnesium alloy AE42, Materials Science & Engineering A, 510-511 (2009) 382-386.
- [45] M. Kerr, N. Chawla, Creep deformation behavior of Sn-3.5Ag solder/Cu couple at small length scales, 52 (2004) 4527-4535.
- [46] B. Chen, S. Moon, X. Yao, G. Bi, J. Shen, J. Umeda, K. Kondoh, Strength and strain hardening of a selective laser melted AlSi10Mg alloy, Scripta Materialia, 141 (2017) 45-49.
- [47] J. Hu, W. Zhang, G. Bi, J. Lu, W. Huo, Y. Zhang, Nanoindentation creep behavior of coarse-grained and ultrafine-grained pure magnesium and AZ31 alloy, Materials Science and Engineering: A, 698 (2017) 348-355.
- [48] K. Kunze, T. Etter, J. Graesslin, V. Shklover, Texture, anisotropy in microstructure and mechanical properties of IN738LC alloy processed by selective laser melting (SLM), Materials Science & Engineering A, 620 (2015) 213-222.
- [49] Z. Li, Z. Li, Z. Tan, D.B. Xiong, Q. Guo, Stress relaxation and the cellular structure-dependence of plastic deformation in additively manufactured AlSi10Mg alloys, International Journal of Plasticity, 127 (2020) 102640.
- [50] J. Wu, X.Q. Wang, W. Wang, M.M. Attallah, M.H. Loretto, Microstructure and strength of selectively laser melted AlSi10Mg, Acta Materialia, 117 (2016) 311-320.
- [51] K. Kempen, L. Thijs, J. Van Humbeeck, J. P. Kruth, Processing AlSi10Mg by selective laser melting: parameter optimisation and material characterisation, Materials Science and Technology, 31

(2015) 917-923.

[52] Z. Xiong, S. Liu, S. Li, Y. Shi, Y. Yang, R. Misra, Role of melt pool boundary condition in determining the mechanical properties of selective laser melting AlSi10Mg alloy, *Materials Science and Engineering: A*, 740 (2019) 148-156.

[53] P. Wei, Z. Wei, Z. Chen, J. Du, Y. He, J. Li, Y. Zhou, The AlSi10Mg samples produced by selective laser melting: single track, densification, microstructure and mechanical behavior, *Applied surface science*, 408 (2017) 38-50.

[54] E. Padovano, C. Badini, A. Pantarelli, F. Gili, F. D'Aiuto, A comparative study of the effects of thermal treatments on AlSi10Mg produced by laser powder bed fusion, *Journal of Alloys and Compounds*, 831 (2020) 154822.

[55] M. Fousová, D. Dvorský, A. Michalčová, D. Vojtěch, Changes in the microstructure and mechanical properties of additively manufactured AlSi10Mg alloy after exposure to elevated temperatures, *Materials Characterization*, 137 (2018) 119-126.

[56] D. Du, J.C. Haley, A. Dong, Y. Fautrelle, D. Shu, G. Zhu, X. Li, B. Sun, E.J. Lavernia, Influence of static magnetic field on microstructure and mechanical behavior of selective laser melted AlSi10Mg alloy, *Materials & Design*, 181 (2019) 107923.

[57] Y. Bai, Y. Yang, Z. Xiao, M. Zhang, D. Wang, Process optimization and mechanical property evolution of AlSiMg0.75 by selective laser melting, *Materials & Design*, 140 (2018) 257-266.

[58] S. Siddique, M. Imran, E. Wycisk, C. Emmelmann, F. Walther, Influence of process-induced microstructure and imperfections on mechanical properties of AlSi12 processed by selective laser melting, *Journal of Materials Processing Technology*, 221 (2015) 205-213.

[59] L. Girelli, M. Tocci, M. Gelfi, A. Pola, Study of heat treatment parameters for additively manufactured AlSi10Mg in comparison with corresponding cast alloy, *Materials Science and Engineering: A*, 739 (2019) 317-328.

[60] Q. Yan, B. Song, Y. Shi, Comparative study of performance comparison of AlSi10Mg alloy prepared by selective laser melting and casting, *Journal of Materials Science & Technology*, 41 (2020) 199-208.

[61] X. Dong, X. Zhu, S. Ji, Effect of super vacuum assisted high pressure die casting on the repeatability of mechanical properties of Al-Si-Mg-Mn die-cast alloys, *Journal of Materials Processing Technology*, 266 (2019) 105-113.